Increased European Heat Waves in Recent Decades in Response to Shrinking Arctic Sea Ice and Eurasian Snow Cover

Ruonan Zhang[1,2], Chenghu Sun[3,4], Jieshun Zhu[5], Renhe Zhang[1] & Weijing Li[6]

[1]Department of Atmospheric and Oceanic Sciences & Institute of Atmospheric Sciences, Fudan University, Shanghai, China

[2]Shanghai Institute of Pollution Control and Ecological Security, Shanghai, China

[3]State Key Laboratory of Severe Weather and Institute of Climate System, Chinese Academy of Meteorological Sciences, Beijing, China

[4]Collaborative Innovation Center on Forecast and Evaluation of Meteorological Disasters, Nanjing University of Information Science & Technology, Nanjing, China

[5]Earth System Science Interdisciplinary Center, University of Maryland, College Park, Maryland, USA

[6]National Climate Center, China Meteorological Administration, Beijing, China

Corresponding author address: Dr. Weijing Li and Chenghu Sun, China Meteorological Administration, No. 46, Zhongguancun Nandajie, Beijing 100081, China. E-mail: liwj@cma.gov.cn; sunch@cma.gov.cn.

Supplementary Note 1. Possible physical mechanisms in reanalysis data

To explore the physical mechanisms responsible for the impacts of ASIC and EASC loss on the frequency of summer heat waves in Europe, we primarily investigated the vertical characteristics of anomalous large-scale atmospheric circulations. Supplementary Figure 1 shows the differences in atmospheric circulation between the high- and low-HW periods. For the mid–high latitudes of the Eurasian continent, the 500 hPa geopotential height (Z500) and 700 hPa geopotential height (Z700) patterns obtained from the reanalysis data are both characterized by a clear zonal "+ - +" wave train and evident lower-tropospheric anticyclonic circulation over Europe (Supplementary Figs. 1a–b). These features are very similar to those at Z200 (Fig. 3a), and the fact that the anomalies in each level are basically co-localized and increase with height suggest that this wave train exhibits a vertical quasi-barotropic structure. Moreover, a stronger meridional temperature gradient (MTG) is evident at 500 hPa in highlatitude Europe (Supplementary Fig. 1c), and it enhances the local U200 and weakens the midlatitude U200 via the thermal wind process. Accompanied by the weakened STEA spreading along the midlatitudes, these large-scale and synoptic-scale circulation anomalies promote the formation of summer blocking ridges in Europe. Under the circumstance, the weather conditions tend to persist, thus increasing the probability and magnitude of summer heat waves in Southern and Eastern Europe (Figs. 1a–b).

Supplementary Note 2. Further simulation results of Arctic sea ice experiments

We designed three pairs of sensitive experiments to explore the individual and combined influences of the ASIC and EASC on summer circulation in Europe, and details of the experimental design are presented in Table 1. Associated with a decline in the ASIC, positive geopotential height anomalies are evident at Z500 and Z700 over Europe and northeast Asia (Supplementary Figs. 2a–b). The low ASIC in spring causes a wave activity flux branch to propagate toward Eastern Europe, which leads to an increase of TMX in Eastern Europe (figure not shown). This warm surface persists to the following summer (Fig. 5b), implying a possibly high HWMId, and simultaneously forms a clear meridional temperature gradient between the pole and midlatitudes (Supplementary Fig. 2c). This stronger meridional temperature gradient enhances the U200 in highlatitude Europe and weakens it in midlatitudes, and this pattern is similar to the spatial pattern in the reanalysis data (Supplementary Fig. 1c) but with smaller amplitude. These simulations confirm the active role of the ASIC in affecting highaltitude European blockings and heat waves in Eastern Europe.

Supplementary Note 3. Further simulation results of Eurasian snow cover experiments

We designed a scheme to obtain a more realistic snow distribution that reflects the snow albedo and hydrological process characteristics. To verify the model's performance in mimicking actual Eurasian snow cover, Supplementary Figure 3a–b shows distributions of the Eurasian snow water equivalent (SWE) differences in spring and summer between the LSNOW and HSNOW experiments. In spring, the significantly lower SWEs are observed in most mid–high latitudes of the Eurasian continent and in the northwestern Tibetan Plateau, with a significantly higher SWE in the southeastern Tibetan Plateau. In summer, the SWE continues to be low in the Far East and the northwestern Tibetan Plateau. These patterns are very similar to the snow cover distribution derived from the observations (Figs. 2g–l). In response, the large-scale "- + - +" zonal wave trains at Z500 and Z700 (Supplementary Figs. 3c–d) are essentially reproduced, with the strongest anomalies generally located in areas where the EASC shrinks. This experiment also reproduces the negative meridional temperature gradient anomalies and the weaker U200 in Southern Europe (Supplementary Fig. 3e). What needs to be emphasized is that a stronger high-pressure ridge (Fig. 3g) and a relatively higher TMX (Fig. 5c) are located over the whole Europe and correspond to the remaining regions with low snow coverage, thus indicating a widespread and stronger amplitude of the impacts of Eurasian snow cover than that in the ensemble-mean fields of the sea ice experiments, which are restricted to Eastern Europe. Relative to the sea ice experiments, the snow cover experiment results are more similar to the reanalysis data in the geographic extent, indicating the role of the EASC in influencing heat waves over all the Southern and Eastern Europe.

Supplementary Note 4. Further simulation results of the combined Arctic sea ice and Eurasian snow cover experiments

In the combined effect experiments, the same negative SWE anomaly distribution in the mid–high latitude of Eurasia and the northwestern Tibetan Plateau (Supplementary Figs. 4a–b) was successfully reproduced. Under the combination of ASIC and EASC loss, the "- + - +" zonal wave trains at Z500 and Z700 (Supplementary Figs. 4c–d) were nearly identical to their observational counterparts and showed a similar high center in geographic extent and amplitude. A decrease of the summer meridional temperature gradient occurs in the same location as in the reanalysis data (Supplementary Fig. 4e), and it directly leads to a weakened U200 at midlatitudes (Fig. 3k). The prevalence of positive height anomalies and slower zonal winds suggests that the anomalous blocking ridge may strengthen or shift to Southern and Eastern Europe in response to the decrease in the ASIC and EASC, thus contributing to more extreme heat waves. These results are inconsistent with the separate sea ice and snow cover experiments, whose variations are generally weaker than those in the combined experiments. Therefore, it can be concluded that these combined experiment results present a closer resemblance to the reanalysis data than the individual experiments, thus presenting more evidence that the combined effects of ASIC and EASC essentially influence more hot summers in Europe.

Supplementary Note 5. CMIP5 models analyzed in this study

We further analyzed the monthly and daily CMIP5 historical and RCP4.5 experiments for the period 1980–2100 from 23 coupled general circulation models based on the availability of ASIC and SWE output. Considering the availability of daily Z500 and TMX output, 13 out of the 23 models were finally chosen for the ensemble-mean analysis: ACCESS1.0, ACCESS1.3, BCC-CSM1.1, CanESM2, CMCC-CMS, CNRM-CM5, GFDL-CM3, GFDL-ESM2G, HadGEM2-CC, HadGEM2-ES, MIROC-ESM, MIROC-ESM-CHEM, and NorESM1-M. Detailed information about the 13 climate models in CMIP5 is shown in Table 2. An analysis of the 13-model ensemble-mean results suggests that both ASIC and EASC will experience rapid declines, and BMI and HWMId will quickly become exacerbated. However, for a robust impact estimation by the reductions in ASIC and EASC in the next century, we must pay attention to the projection uncertainties caused by an insufficient number of CMIP5 model ensemble members. Considering that climate models with daily Z500 datasets are limited, each model should have more members to generate a more robust estimate of the blocking response to future ASIC and EASC reductions. Such a large amount of ensemble projections would contribute to deriving convincing conclusions on potential further changes in European summer blockings and heat waves.

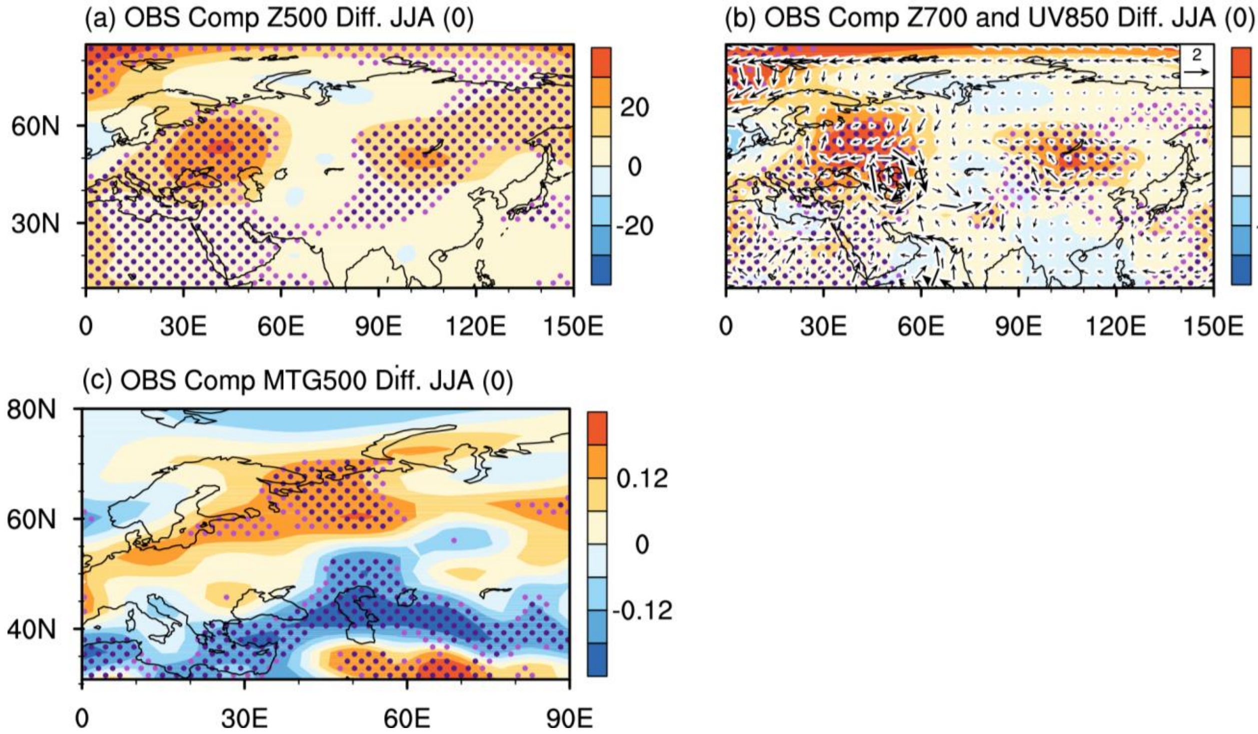

Supplementary Figure 1. Composite differences in the JJA (a) 500 hPa geopotential height, (b) 700 hPa geopotential height and 850 hPa horizontal wind, and (c) 500 hPa meridional temperature gradients (shadings) between high- and low-HW periods. Differences significantly exceeding 90% and 95% confidence levels are marked by light and dark dots, respectively.

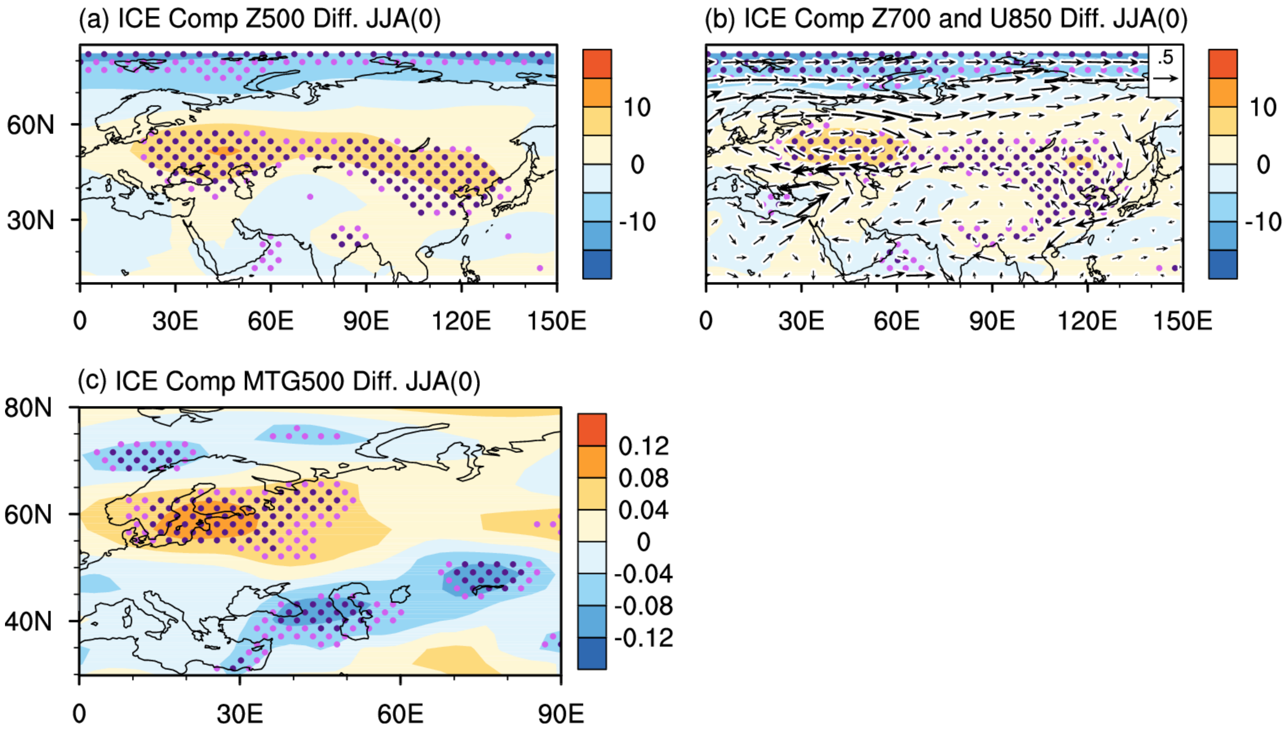

Supplementary Figure 2. Similar to Supplementary Fig. 1 but for the simulated composite differences between the LICE and HICE experiments.

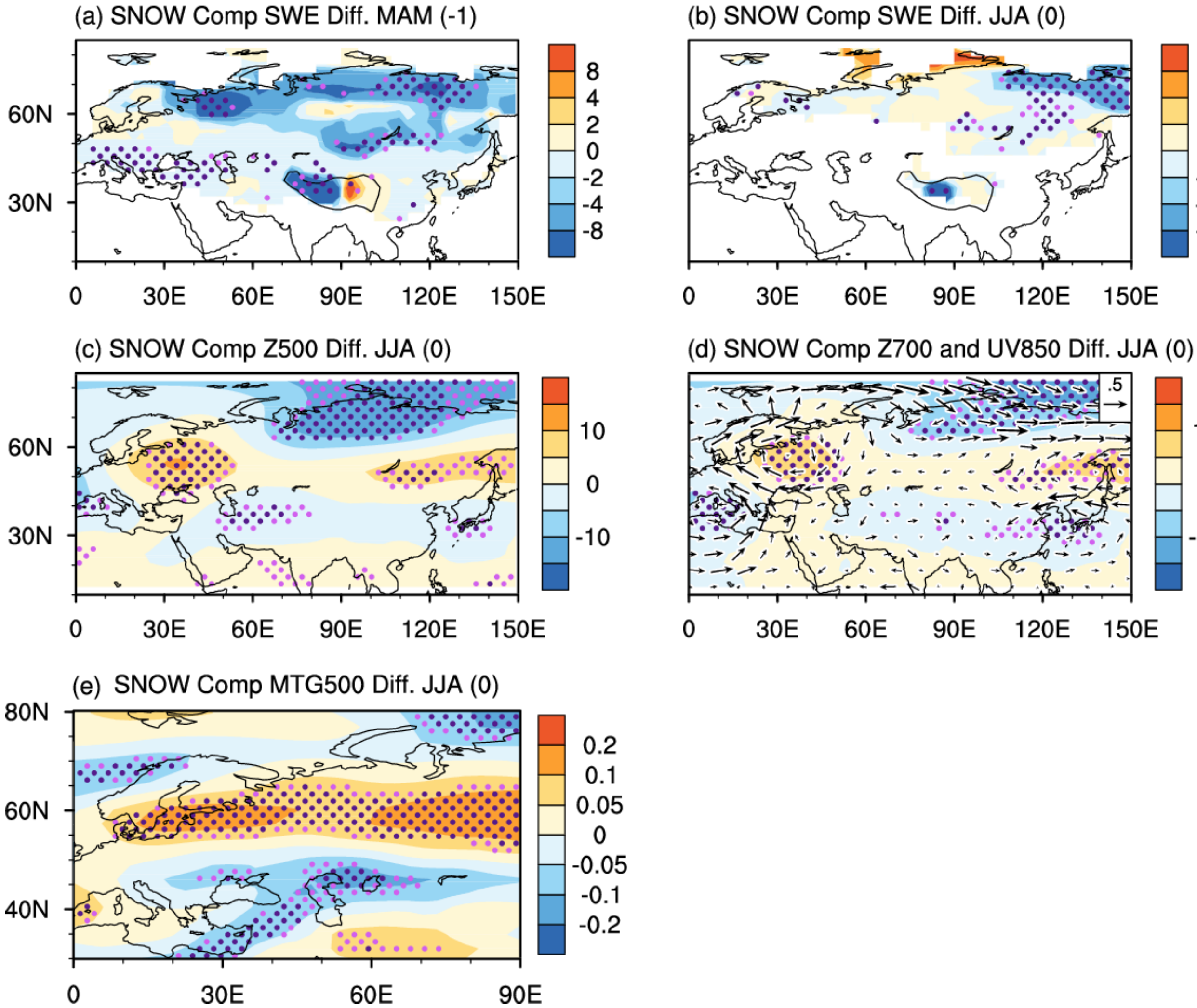

Supplementary Figure 3. Simulated composite differences between the LSNOW and HSNOW experiments. (a) MAM and (b) JJA Eurasian snow water equivalent (SWE), (c) JJA 500 hPa geopotential height, (d) JJA 700 hPa geopotential height and 850 hPa horizontal wind, and (e) 500 hPa meridional temperature gradients. Differences significantly exceeding 90% and 95% confidence levels are marked by light and dark dots, respectively.

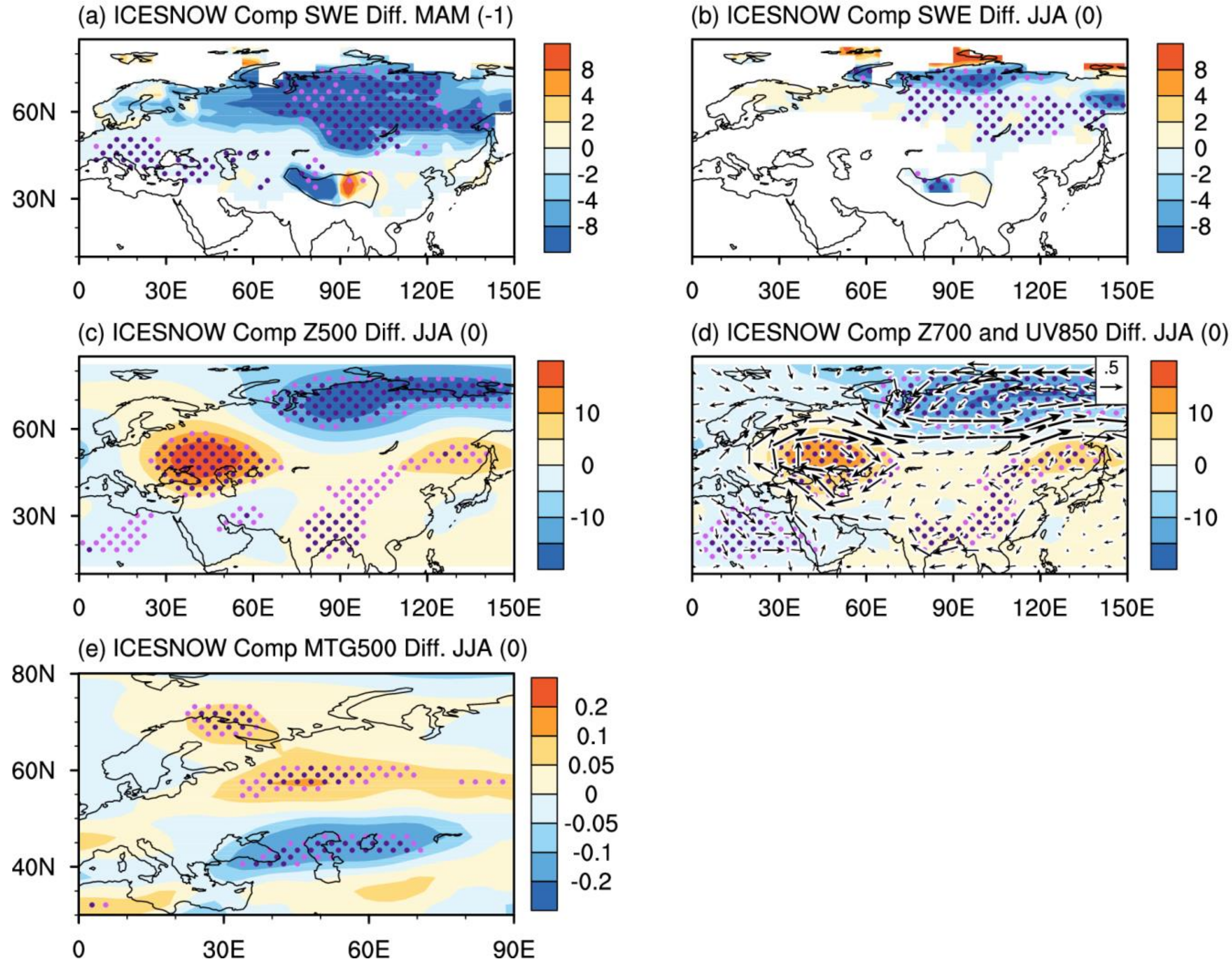

Supplementary Figure 4. Similar to Supplementary Fig. 3 but for the simulated composite differences between the LICESNOW and HICESNOW experiments.

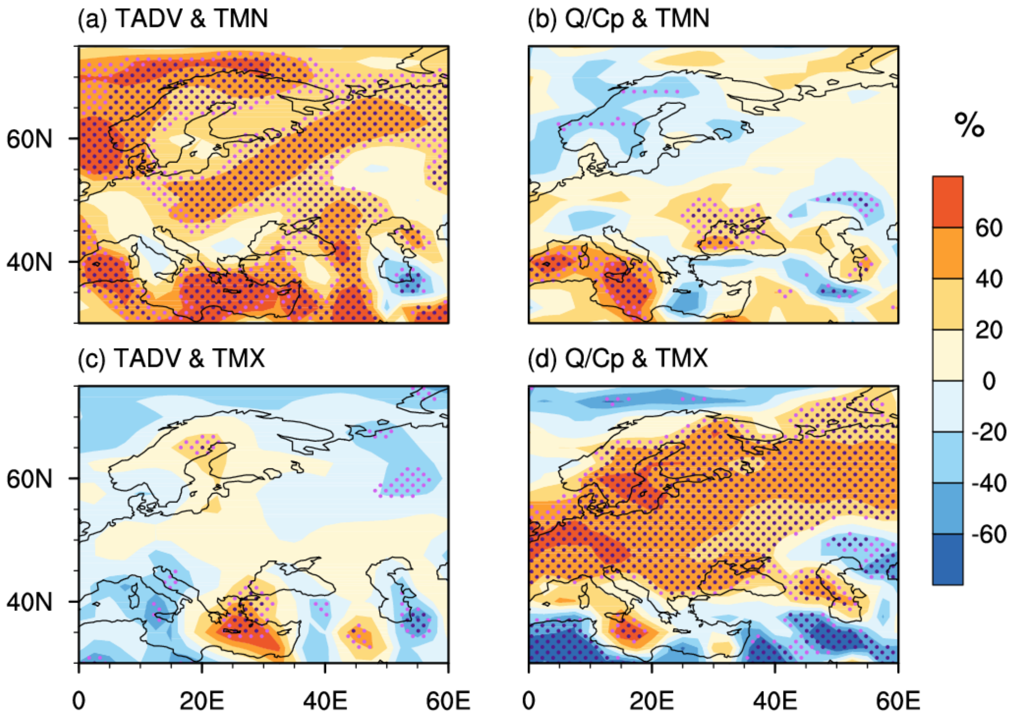

Supplementary Figure 5. The (a-b) mean and (c-d) maximum temperature variances of the NCEP/NCAR reanalysis explained by the temperature advection and the heat flux term. The heat flux term is defined by turbulent heat flux divided by specific heat at constant pressure (Cp). Correlation coefficients significantly exceeding 90% and 95% confidence levels are shown as light and dark dots, respectively.

Supplementary Table 1. Experimental designs for CAM3.1

Experiments		Anomalous forcings	Integration period	Simulation results
ICE	LICE	2003–2015 mean MAM and JJA ASIC anomalies	50 years	LICE-HICE
	HICE	1982–1997 mean	50 years	
SNOW	LSNOW	Halved MAM and JJA snowfall rate over the Eurasian continent	50 years	LSNOW-HSNOW
	HSNOW	Doubled snowfall rate	50 years	
ICESNOW	LICESNOW	Both LICE and LSNOW	50 years	LICESNOW-HICESNOW
	HICESNOW	Both HICE and HSNOW	50 years	

Supplementary Table 2. Detailed information on the 13 climate models in CMIP5. √ indicates that the ASIC and EASC fields are available and √* indicates that the daily 500 hPa geopotential height and maximum surface air temperature are available and were used in the present study.

	Climate model	Country	Resolution	Integration period	Variables			
					ASIC	SWE	Zg	TMX
01	ACCESS1-0	Australia	192×145	1850–2100	√*	√*	√*	√*
02	ACCESS1-3	Australia	192×145	1850–2100	√*	√*	√*	√*
03	BCC-CSM1.1	China	128×64	1850–2099	√*	√*	√*	√*
04	BNU-ESM	China	128×64	1850–2100	√		√	√
05	CanESM2	Canada	128×64	1850–2100	√*	√*	√*	√*
06	CESM1-BGC	US	288×192	1850–2100	√	√		√
07	CESM1-CAM5	US	288×192	1850–2100	√	√		√
08	CMCC-CM	Italy	480×240	1850–2100	√			√
09	CMCC-CMS	Italy	192×96	1850–2100	√*	√*	√*	√*
10	CNRM-CM5	France	256×128	1850–2100	√*	√*	√*	√*
11	CSIRO-MK3.6	Australia	192×96	1850–2100	√	√		√
12	GFDL-CM3	US	144×90	1860–2100	√			
13	GFDL-ESM2G	US	144×90	1861–2100	√*	√*	√*	√*
14	GFDL-ESM2M	US	144×90	1861–2100	√*	√*	√*	√*
15	GISS-E2-R	US	144×90	1850–2100	√	√		

16	HadGEM2-CC	UK	192×145	1859–2100	√*	√*	√*	√*
17	HadGEM2-ES	UK	192×145	1884–2100	√*	√*	√*	√*
18	INMCM4	Russia	180×120	1850–2100	√	√		√
19	MIROC-ESM	Japan	128×64	1850–2100	√*	√*	√*	√*
20	MIROC-ESM-CHEM	Japan	128×64	1850–2100	√*	√*	√*	√*
21	MIROC5	Japan	256×128	1850–2100	√	√		√
22	NorESM1-M	Norway	144×96	1850–2100	√*	√*	√*	√*
23	NorESM1-ME	Norway	144×96	1850–2100	√	√		